Journal of Materials Chemistry A

ROYAL SOCIETY OF CHEMISTRY

PAPER

View Article Online
View Journal

Cite this: DOI: 10.1039/d5ta10085b

Proton conductivity of mesoporous aluminum organophosphonate enhanced by the affinity of an integral organic linker to water molecules

Takahiro Ami,[a] Kouki Oka, *[abc] Hitoshi Kasai [a] and Tatsuo Kimura *[d]

The precise design of aluminophosphate (AlPO)-based frameworks is quite promising for improving the smooth transport of protons at surfaces with abundant sites, such as free phosphoric acid (P–OH) groups and water (H_2O) molecules attached to tetrahedral AlO_4 units. Our latest study has demonstrated that enhancing surface hydrophobicity by embedding bulky aromatic groups, such as a phenylene (–C_6H_4– or –Ph–) linker, is essential for improving the stability of aluminum organophosphonate (AOP)-based frameworks. However, such strong hydrophobicity did not seem suitable for amplifying the proton conduction because the length of proton hopping was increased by the presence of bulky organic linkers. In this study, we suggest rational guidelines to aid the design of molecular structures with enhanced proton conductivity inside surfactant-assisted mesopores, especially at the surfaces of AOP-based frameworks. Two AOP-type materials containing a biphenyl (–C_6H_4–C_6H_4– or –BP–) group, with increased hydrophobicity, and a hydroquinonyl (–$C_6H_2(OH)_2$– or –HQ–) group, which facilitates the proton conduction pathway, were prepared as AOP–BP and AOP–HQ, respectively, using Pluronic P123 ($EO_{20}PO_{70}EO_{20}$). Consequently, the AOP–HQ-type mesoporous material showed a superprotonic conductivity of 1.31×10^{-2} S cm^{-1} under 95% RH at 90 °C. The HQ linker, which provides abundant and additional –OH groups over the hydrophobic –Ph– linker, promotes the formation of a continuous network of H_2O molecules over the entire surface, leading to efficient proton conduction through the Grotthuss mechanism.

Received 10th December 2025
Accepted 18th March 2026

DOI: 10.1039/d5ta10085b

rsc.li/materials-a

1. Introduction

High-performance proton-conducting materials are required for the design of effective electrochemical devices for energy conversion and environmental monitoring[1–3] as well as for humidity and hydrogen sensors.[4,5] The performance of such devices is critically determined by the efficiency of proton migration,[6,7] necessitating chemically stable and highly proton-conducting materials. Highly porous materials have recently emerged as potential candidates for new classes of proton conductors.[8–12] According to their structural features, *e.g.*, well-defined pores and high specific surface areas, proton carriers such as water (H_2O) molecules are accommodated smoothly inside the pores, thereby enabling the formation of an efficient proton-transport pathway.[13–17] In general, proton conduction inside open pores proceeds by two principal routes: proton hopping (Grotthuss) and proton-carrier diffusing (vehicle) mechanisms.[18,19] The contribution of these mechanisms to efficient proton conduction depends on factors such as the hydrophilicity/hydrophobicity of the pore surfaces and the location of functional groups.[20–22] Recent studies have also demonstrated that the architecture of pores, the polarity of the framework, and the design of functional groups are significant factors for regulating mass and ion transport properties.[23–27] Accordingly, a comprehensive understanding of the interrelation among the porous structure, surface properties and humidity environment is critical to developing rational guidelines for improving the proton conductivity.

Aluminophosphate (AlPO)-type materials, consisting of tetrahedral AlO_4 and PO_4 units, are promising frameworks for the precise design of high-performance proton-conducting materials. Their abundant free phosphoric acid (P–OH) groups serve as excellent proton sources.[28] A first layer of H_2O molecules that adsorb on the hydrophilic AlPO-based framework can be utilized for the formation of hydrogen-bonded networks of H_2O molecules.[28–31] To make full use of such structural features, supramolecular-mediated synthesis using amphiphilic organic compounds, such as alkyltrimethylammonium (C_nTMA) surfactants and polymeric triblock

[a]Institute of Multidisciplinary Research for Advanced Materials, Tohoku University, 2-1-1 Katahira, Aoba-ku, Sendai, Miyagi 980-8577, Japan

[b]Carbon Recycling Energy Research Center Ibaraki University, 4-12-1 Nakanarusawa, Hitachi, Ibaraki 316-8511, Japan

[c]Deuterium Science Research Unit, Center for the Promotion of Interdisciplinary Education and Research Kyoto University, Yoshida, Sakyo-ku, Kyoto 606-8501, Japan. E-mail: oka@tohoku.ac.jp

[d]National Institute of Advanced Industrial Science and Technology (AIST), Sakurazaka, Moriyama-ku, Nagoya 463-8560, Japan. E-mail: t-kimura@aist.go.jp

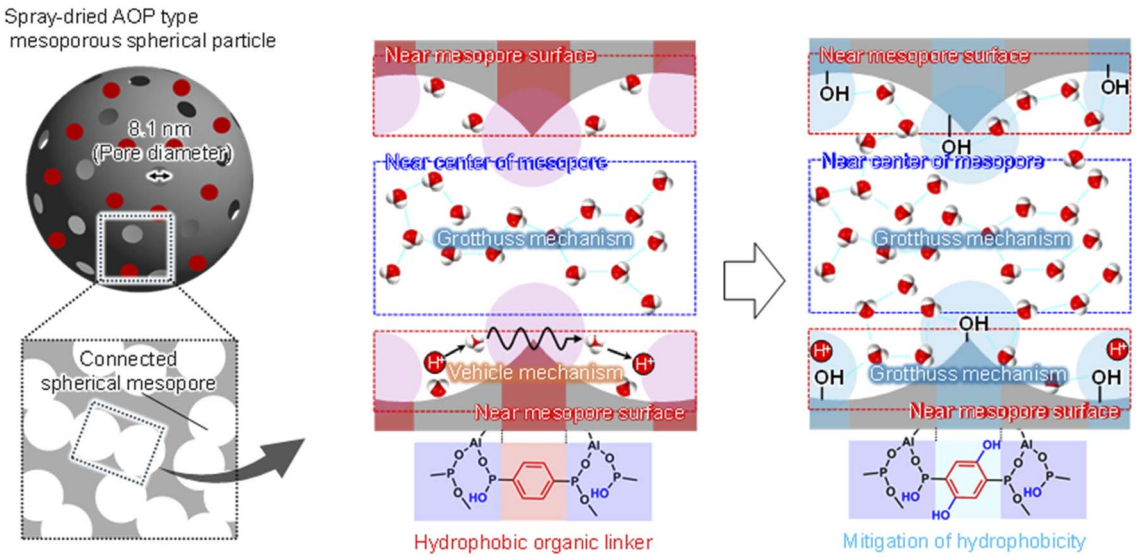

Fig. 1 AOP–BP- and AOP–HQ-type mesoporous materials. Schematic of the designed proton conduction pathway near the surfaces of the AOP-based frameworks with non-interactive –BP– and weakly-interactive –HQ– linkers.

copolymers (*e.g.*, $EO_nPO_mEO_n$), is quite attractive for constructing highly porous AlPO-type materials.[32] The open channels of the resultant AlPO-type mesoporous materials are helpful for the smooth diffusion of H_2O molecules acting as proton carriers, and endow the materials with particularly high potential compared with reported inorganic proton conductors.[33] We have so far succeeded in extending this approach to the preparation of aluminum organophosphonate (AOP)-type materials as the first example of non-silica-based hybrid mesoporous structures.[34–36] The incorporation of organic linkers into AlPO-based frameworks enhances the structural stability of the mesopores and enables the precise control of the surface properties according to the size and functionality of the organic linker.[33] We have then demonstrated the proton conduction mechanism, which is critically tuned through the design of the surface environment of the AOP-type framework.[33]

The rational design of organic linkers (*i.e.*, the main organic moieties and functional groups) to tune interactions between H_2O molecules and organic surfaces and hydrogen-bonded networks of H_2O molecules is important for the smooth transportation of protons. To achieve stable operation and evaluate the proton conductivity of AOP-type materials under high-humidity conditions (*e.g.*, 95% RH) at high temperature (*e.g.*, 90 °C), hydrophobic and bulky organic groups such as phenylene ($–C_6H_4–$ or –Ph–) linker should be introduced inside the AlPO-based frameworks.[33] However, the presence of such hydrophobic organic linkers disturbs the hydrogen-bonded networking of H_2O molecules at the nearby surface of the organic groups, resulting in the reduction of the space for the proton conduction. To maintain the proton conductive space, the addition of functional groups and interaction sites on the aromatic linkers organic linkers is quite reasonable. The importance of the molecular structure of the organic linkers has also been demonstrated by using crystalline porous materials, such as metal–organic frameworks (MOFs).[37]

In this study, we enhance the surface hydrophobicity by incorporating bulky biphenyl ($–C_6H_4–C_6H_4–$ or –BP–) groups to confirm the proton conduction mechanism near the surface of the AOP-based frameworks. As another organic linker design, the hydrophobic organic linker was modified with hydroxyl (–OH) groups to offer weak interactions with H_2O molecules over the organic groups, which is central to develop the rational guideline for increasing the proton transport (Fig. 1). Considering the proton conduction by H_2O molecules, the proton hopping Grotthuss mechanism is predominant inside uniform mesopores, and it is more important for maximizing the total proton conductivity than the proton carrier diffusing vehicle mechanism near the surfaces of AOP-based frameworks. The introduction of hydroquinonyl ($–C_6H_2(OH)_2–$ or –HQ–) groups enables the formation of hydrogen-bonded networks of H_2O molecules near the surface in addition to those generated by bulk H_2O inside the mesopores.

2. Experimental section

2.1 Materials

Pluronic P123 ($EO_{20}PO_{70}EO_{20}$) was obtained from Sigma-Aldrich and used for the spray-dried synthesis of sphere-shaped AOP-type mesoporous materials. Tetraethyl 4,4′-biphenylenebisphosphonate ($(H_5C_2O)_2OP\text{-}Ph\text{-}Ph\text{-}PO(OC_2H_5)_2$, –BP–) and tetraethyl 2,5-dihydroxy-1,4-phenylenebisphosphonate ($(H_5C_2O)_2OP\text{-}C_6H_2(OH)_2\text{-}PO(OC_2H_5)_2$. –HQ–) were purchased from Epsilon Chemie. Anhydrous aluminum chloride ($AlCl_3$) and dehydrated ethanol (EtOH) were obtained from Wako Chemical Co. Phosphoric acid (85% H_3PO_4) was purchased from Kanto Chemical Co. Inc.

2.2 Synthesis of mesoporous AOP-type materials

According to our previous studies,[37–39] partly acidified bisphosphonate compounds were utilized for the synthesis of the

two AOP-type mesoporous materials, named AOP–BP and AOP-HQ. The bisphosphonate esters $(H_5C_2O)_2OP\text{-}BP\text{-}PO(OC_2H_5)_2$ (10.66 g, 25 mmol) and $(H_5C_2O)_2OP\text{-}HQ\text{-}PO(OC_2H_5)_2$ (9.55 g, 25 mmol) were treated at around 90 °C with an aqueous solution of hydrochloric acid (5 M HCl (10 mL) plus H_2O (10 mL)) in a closed bottle. After stirring at the same temperature for 6 h, the resultant bisphosphonate compounds were recovered by heating in an open Petri dish. For example, an acidification degree of $(H_5C_2O)_2OP\text{-}HQ\text{-}PO(OC_2H_5)_2$ was evaluated to be 56.3% by ^{31}P NMR (Fig. S1). The clear precursor solutions for the aerosol-assisted synthesis of AOP–BP and AOP–HQ were prepared as follows. Anhydrous $AlCl_3$ powder (0.67 g) was added in small amounts to an ethanolic solution (10 mL with H_2O (1 mL)) of a partially acidified biphenyl bisphosphonate compound (1.76 g), stirred for 15 min and combined with another ethanolic solution of Pluronic P123 (1.60 g, 10 mL of EtOH and 1 mL of H_2O). Anhydrous $AlCl_3$ powder (0.16 g) was added slowly to an ethanolic solution (10 mL with H_2O (1 mL)) of a partially acidified hydroquinonyl bisphosphonate compound (0.20 g), stirred for 15 min and mixed with another ethanolic solution of Pluronic P123 (0.39 g, 10 mL of EtOH and 1 mL of H_2O). Referring to our synthetic conditions,[38] the precursor solutions were stirred for another 120 min and spray-dried at 110 °C (Yamato Scientific Co., Spray Dryer GB22). All the powder samples were treated three times in dehydrated acetone at 90 °C for around 16 h in a Teflon tube, facilitating the removal of polymeric surfactant molecules.[40,41]

2.3 Characterizations

Fourier-transform infrared (FT-IR) spectra were recorded on an IRSpirit spectrophotometer (Shimadzu, Japan). FT-IR spectra, focusing on the O–H stretching region associated with hydrogen-bonded H_2O molecules, were also collected under high humidity conditions at different temperatures. Low-angle X-ray diffraction (XRD) patterns were measured with a Rigaku RINT 2100 diffractometer with monochromated Fe Kα radiation (40 kV, 30 mA). After the samples were heated at 80 °C for 3 h under vacuum, nitrogen (N_2) and water (H_2O) adsorption–desorption isotherms were measured at −196 °C and 25 °C, respectively, with a BELSORP-max X (MicrotracBEL, Japan). Specific surface areas were calculated by the Brunauer–Emmett–Teller (BET) method using adsorption branches (described as N_2–S_{BET}). Total pore volumes were estimated by using the amounts adsorbed at around $P/P_0 = 0.95$ (expressed as V_{total}). The pore size distribution curves were drawn using the Barrett–Joyner–Halenda (BJH) method using desorption branches. The surface properties of the AOP-based frameworks were roughly considered by examining the adsorption behavior of H_2O molecules. H_2O adsorption measurements were also performed at 40 °C to calculate the isosteric heat of adsorption (Q_{st}), which reflects the strength of interaction between H_2O molecules and material surfaces as a thermodynamic indicator of surface hydrophilicity. Liquid-phase ^{31}P NMR spectra were recorded with a Bruker AVANCE III 400 (400 MHz) spectrometer. X-ray photoelectron spectroscopy (XPS) data were obtained with a ULVAC-PHI PHI5000 VersaProbe II.

Proton conductivity was measured by using pelletized samples pressed under the same conditions with a constant pressure (30 MPa) for 10 s in a cylindrical die (surface area = 0.385 cm^2). AC impedance measurements were performed with an ALS 760 E dual electrochemical analyzer (BAS Ltd) in the frequency range from 10^{-1} to 10^6 Hz with 0.01 V (amplitude voltage); the relative humidity (RH) and temperature were controlled by using an IW223 incubator (Yamato Scientific Co.). The resistance value was estimated from the equivalent circuit fit (Fig. S2) of the first semi-circle using pyZwx.[33] The activation energy for proton transport was calculated by using the data at a constant RH (95%) using the Arrhenius equation $\sigma = (\sigma_0/T) \times \exp(-E_a/kT)$, where σ is the conductivity, σ_0 is a pre-exponential factor, T is the temperature, k is the Boltzmann constant, and E_a is the activation energy. The proton conductivity was then calculated as the average of the resistance values obtained from three repeated measurements under the same conditions.

3. Results and discussion

AOP-type mesoporous materials, where BP and HQ linkers are distributed inside the AlPO-like frameworks, can be prepared through the evaporation-induced self-assembly (EISA) process induced by spray-drying the precursor solutions in the presence of Pluronic P123. In addition to our structural model to improve the proton conductivity inside mesopores by the presence of hydrophobic organic groups,[33] we also aimed to enhance the proton conductivity through the precise design of the AOP-based framework, as illustrated in Fig. 1. Under high humidity conditions, the inner spaces of the surfactant-assisted mesopores are occupied by enough H_2O molecules for the protons to be transported through the hydrogen-bonding network of H_2O molecules. However, H_2O molecules cannot move smoothly at the outermost surfaces because of the strong ligation to inorganic AlO_4 units. Considering the increase in surface hydrophobicity caused by the incorporation of organic groups such as the BP linker rather than the phenyl (–Ph–) linker, protons may diffuse at a longer distance beyond the organic linker from an inorganic unit to an adjacent one. Accordingly, an accessible point by H_2O molecules should be designed over the organic linker to reduce the distance to diffuse. Such a precise functional design of AOP-based framework is promising for increasing the total proton conduction.

3.1 Synthesis of AOP–BP-type mesoporous material and its proton conductivity

The FT-IR spectra of AOP–BP-type materials prepared using Pluronic P123 before and after treatment in dehydrated acetone are shown in Fig. 2a. Before the removal of Pluronic P123, several bands attributed to $EO_nPO_mEO_n$-type molecules were detected at 2972–2869 cm^{-1}, 1654 cm^{-1} and 1476 cm^{-1}. The broad bands centered at 2972 cm^{-1} (O–H stretching vibration) and 1654 cm^{-1} (O–H bending vibration) were assigned to free phosphoric acids (P–OH and P═O), hydroxyl (–OH) groups of Pluronic P123 and adsorbed H_2O molecules. The bands at 1654 cm^{-1} and 1476 cm^{-1} were ascribed to the stretching and

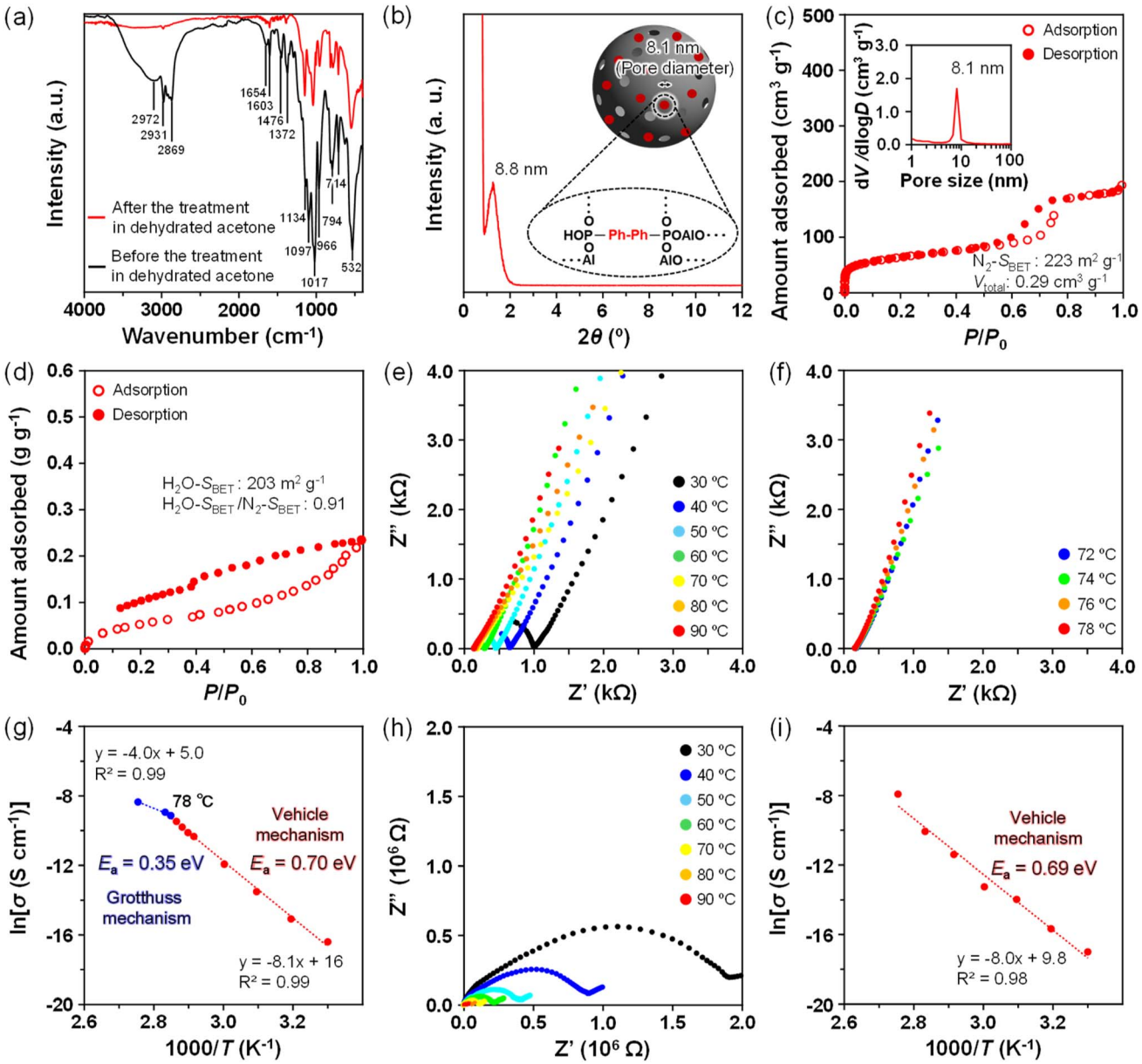

Fig. 2 Analysis of the AOP–BP-type mesoporous material. (a) FT-IR spectra before and after treatment with dehydrated acetone. (b) Low-angle XRD pattern with a schematic structural model. (c) N_2 adsorption–desorption isotherms with the corresponding pore size distribution curve. (d) H_2O adsorption–desorption isotherms. (e) Impedance spectra of the disk-shaped pellet at temperatures ranging from 30 °C to 90 °C. (f) Impedance spectra from 72 °C to 78 °C under 95% RH. (g) Arrhenius plot of the proton conductivity under 95% RH. (h) Impedance spectra from 30 °C to 90 °C under 60% RH. (i) Arrhenius plot of the proton conductivity under 60% RH.

bending vibrations of C–H due to the presence of Pluronic P123. The comparison of the spectra before and after treatment in dehydrated acetone clearly revealed the complete removal of the $EO_nPO_mEO_n$-type molecules. A weak band was still observed around 2900 cm^{-1} due to the C–H stretching vibration, indicating the retention of the original ester groups in the partially acidified bisphosphonate precursor in the final AOP–BP-type mesoporous material. Strong bands that can be attributed to the P=O stretching vibration were also observed at around 1000 cm^{-1} in the spectra of the AOP–BP-type materials. Other bands in the ranges of 1000–800 cm^{-1} and 700–500 cm^{-1} were assigned to the asymmetric and symmetric stretching vibrations of Al–O–P bonds, respectively. The C=C stretching vibration of aromatic rings was also detected at 1603 cm^{-1} and 1372 cm^{-1}, indicating the presence of aromatic linkers in the final AOP–BP framework (Table S1). The low-angle XRD pattern of AOP–BP after the removal of Pluronic P123 showed the presence of a distinct diffraction peak at $2\theta = 1.26°$ (Fig. 2b), corresponding to a d-spacing of 8.8 nm. The N_2 adsorption–desorption isotherm was type IV (Fig. 2c), indicating the presence of abundant uniform mesopores with an average pore diameter of 8.1 nm.[42] According to our recent findings during

the preparation of AOP–BP, the Pluronic P123 templated mesopores are spherical and distributed over the whole of the aerosol-assisted spherical particles.[43] The specific surface area and the total pore volume were calculated to be 223 $m^2 g^{-1}$ and 0.29 $cm^3 g^{-1}$, respectively.

The H_2O adsorption–desorption isotherm of AOP–BP seemed to be type IV (Fig. 2d), being similar to those reported for AOP-type mesoporous materials containing hydrophobic –Ph– groups.[33] In the adsorption process, H_2O molecules can adsorb even in the very low relative humidity (RH) region ($P/P_0 <$ 0.04) because of the strong interaction with AlO_4 as the first layer of H_2O molecules. A multi-layer adsorption of H_2O molecules was then started through interactions with the attached H_2O molecules and subsequent formation of H_2O clusters in the region of $P/P_0 = 0.03$–0.88, followed by a gradual increase in the adsorption in the region of humidity above $P/P_0 \simeq 0.88$. In the desorption process, a large hysteresis loop was observed by several interactions between H_2O molecules and the surfaces (*e.g.*, AlO_4 units and free P–OH groups) even in the presence of bulky and hydrophobic BP linkers. The H_2O–S_{BET} and H_2O–S_{BET}/N_2–S_{BET} values of AOP–BP were calculated to be 203 $m^2 g^{-1}$ and 0.91, respectively, being the smallest among our previous AOP-type mesoporous materials.[33] The total amount of adsorbed H_2O (0.24 g g^{-1}) was almost identical to the total pore volume (0.29 $cm^3 g^{-1}$) calculated from the N_2 adsorption data, suggesting that the mesopores were fully filled with H_2O molecules under saturated humidity ($P/P_0 = 1.0$).

The proton conductivity of AOP–BP was measured at temperatures in the range of 30 °C to 90 °C under high humidity conditions using electrochemical impedance spectroscopy (EIS). The Nyquist and Arrhenius plots were constructed (Fig. 2e, f and g and the corresponding data in Table 1) for mesopores filled with H_2O molecules (95% RH). The activation energy (E_a) was calculated to be 0.70 eV below 78 °C and 0.35 eV above 78 °C. The results indicate that protons are conducted predominantly through the vehicle mechanism below 78 °C at sufficiently high RH conditions and through the Grotthuss mechanism at higher temperatures. As described in our previous work on the proton conductivity of AOP-type mesoporous materials,[33] the temperature-dependence of proton conduction is induced by the introduction of hydrophobic organic linkers. The transition temperature of the highly hydrophobic AOP–BP (78 °C) was higher than those observed for AOP–CH_2 (32 °C), AOP–C_2H_4 (40 °C) and AOP–Ph (52 °C). The resultant proton conductivity of AOP–BP reached 2.07 × 10^{-3} S cm^{-1} at 90 °C (95% RH), which is comparable with that of typical AOP-type mesoporous proton-conducting materials (Table S2).[33] To clarify the proton conduction mechanism near the surfaces, the proton conductivity was measured under reduced humidity conditions (Fig. 2h). The transition of the proton conduction mechanism was not observed at 60% RH, revealing that protons were transported by the vehicle mechanism (E_a; 0.69 eV) in all temperature ranges (Fig. 2i).

Table 1 Proton conductivities of the AOP–BP- and AOP–HQ-type mesoporous materials

Temperature (°C)	Proton conductivity (S cm^{-1})			
	AOP–BP		AOP–HQ	
	95% RH	60% RH	95% RH	60% RH
30	3.70×10^{-5}	6.80×10^{-8}	9.12×10^{-4}	1.69×10^{-6}
40	7.16×10^{-5}	1.32×10^{-7}	1.84×10^{-3}	2.50×10^{-6}
50	1.57×10^{-4}	3.08×10^{-7}	3.15×10^{-3}	3.69×10^{-6}
60	3.46×10^{-4}	4.44×10^{-7}	5.17×10^{-3}	5.33×10^{-6}
70	7.66×10^{-4}	1.12×10^{-6}	6.80×10^{-3}	7.25×10^{-6}
72	8.56×10^{-4}	—	—	—
74	1.00×10^{-3}	—	—	—
76	1.18×10^{-3}	—	—	—
78	1.40×10^{-3}	—	—	—
80	1.54×10^{-3}	2.17×10^{-6}	9.62×10^{-3}	1.19×10^{-5}
90	2.07×10^{-3}	6.38×10^{-6}	1.31×10^{-2}	1.91×10^{-5}

3.2 Synthesis of AOP–HQ-type mesoporous material and its proton conductivity

To mitigate the strong suppression of the Grotthuss mechanism, we designed AOP–HQ as another AOP-type material in which interactive –OH groups were introduced onto the hydrophobic –Ph– group. The FT-IR spectra of AOP–HQ exhibited typical bands corresponding to the formation of the AOP-type mesoporous framework and the presence of Pluronic P123 (Fig. 3a and Table S1), which appeared in regions similar to those observed for AOP–BP. A residual band at 1643 cm^{-1}, attributed to the O–H bending vibration of the HQ linker, was observed even after the removal of Pluronic P123. A comparison between AOP–HQ and the partially acidified bisphosphonate compound (Fig. S3) was conducted based on the XPS data. A clear Al 2p signal was observed for AOP–HQ, suggesting the presence of Al species in the resultant AOP–HQ framework. In addition, the O 1s and P 2p signals of AOP–HQ shifted from those of the partially acidified bisphosphonate compound, being related to the change of the chemical environments by the formation of Al–O–P bonds. The presence of a distinct diffraction peak was confirmed at $2\theta = 1.26°$ ($d = 8.8$ nm) in the low-angle XRD pattern of AOP–HQ after the removal of Pluronic P123 (Fig. 3b). The N_2 adsorption–desorption isotherm exhibited a type IV behavior with a narrow pore-size distribution centered at 8.1 nm (Fig. 3c). The specific surface area and the total pore volume were 316 $m^2 g^{-1}$ and 0.42 $cm^3 g^{-1}$, respectively.

The H_2O isotherm of AOP–HQ showed a type IV behavior, but the adsorption of H_2O molecules already started in the very low RH region ($P/P_0 < 0.05$), followed by multilayer adsorption in the humidity range $P/P_0 = 0.05$–0.40 (Fig. 3d). A steep increase by capillary condensation was also observed in the higher humidity region ($P/P_0 > 0.6$) with a larger hysteresis loop due to the enhanced interactions with H_2O molecules. The H_2O–S_{BET} and H_2O–S_{BET}/N_2–S_{BET} values of AOP–HQ were calculated to be 487 $m^2 g^{-1}$ and 1.54, respectively. The H_2O–S_{BET}/N_2–S_{BET} value was lower than that of pure AlPO (1.87) and higher than those of AOP-type mesoporous materials modified with methylene (1.41, $–CH_2–$) and unmodified phenylene (1.05, –Ph–) groups.[33] The

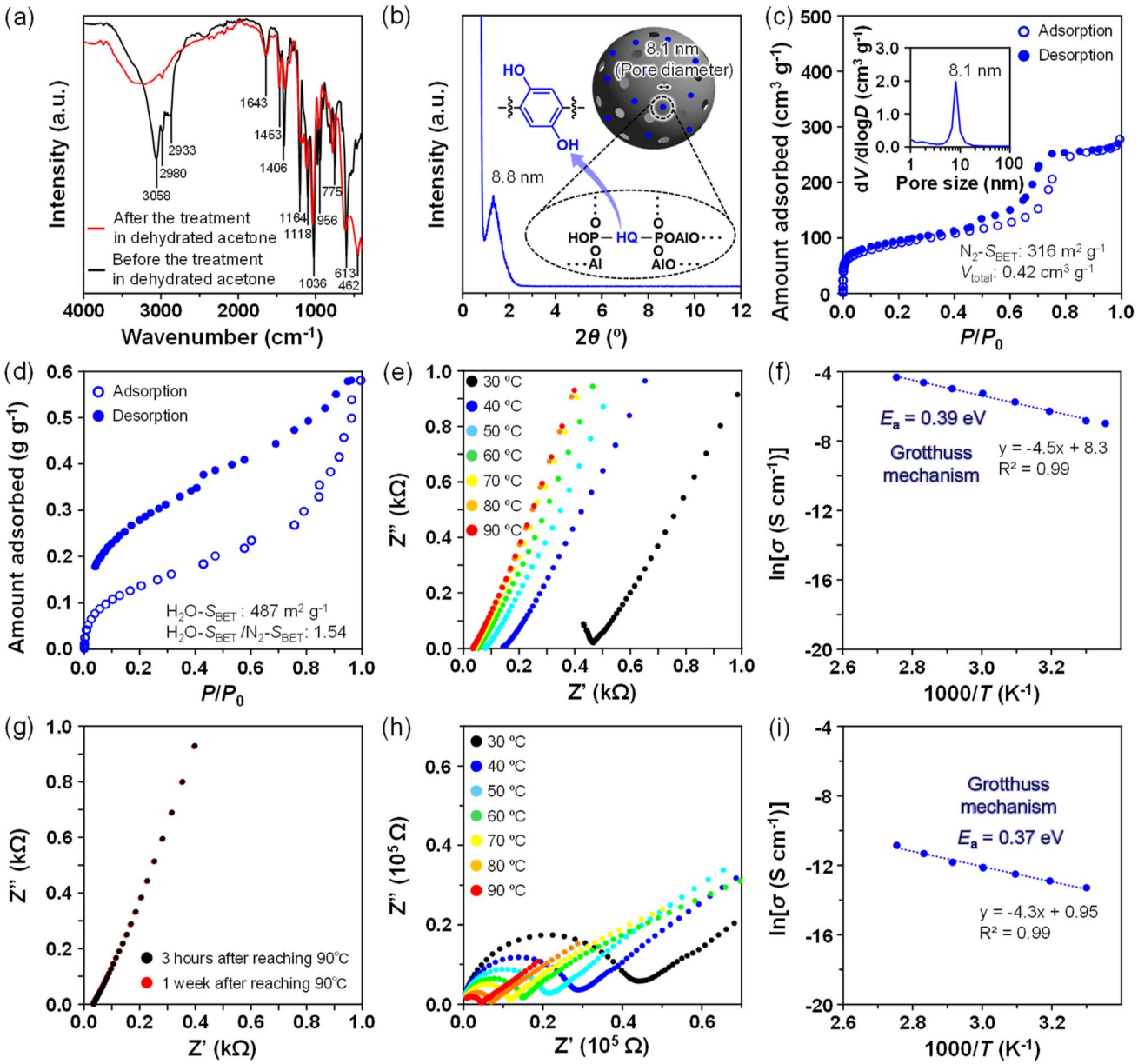

Fig. 3 Analysis of the AOP–HQ-type mesoporous material. (a) FT-IR spectra before and after treatment with dehydrated acetone. (b) Low-angle XRD pattern with a schematic structural model. (c) N_2 adsorption–desorption isotherms with the corresponding pore-size distribution curve. (d) H_2O adsorption–desorption isotherms. (e) Impedance spectra of the disk-shaped pellet at temperatures ranging from 30 °C to 90 °C. (f) Arrhenius plot of the proton conductivity under 95% RH. (g) Impedance spectra of the disk-shaped pellet at 3 hours and 1 week after reaching 90 °C. (h) Impedance spectra from 30 °C to 90 °C under 60% RH. (i) Arrhenius plot of the proton conductivity under 60% RH.

adsorbed amount of H_2O reached 0.58 g g^{-1} at $P/P_0 = 1.0$, which is slightly larger than the total pore volume ($V_{total} = 0.42$ cm^3 g^{-1}). The adsorption measurements by using H_2O vapor clearly revealed that the surface property of AOP–HQ (reduced hydrophobicity, designed hydrophilicity) was totally different from that of AOP–BP (strong hydrophobicity). The modification by functional groups that can interact with H_2O molecules is a powerful strategy to reduce the original hydrophobicity of the aromatic linkers.

The proton conductivity of AOP–HQ was also evaluated under the same conditions applied for AOP–BP, affording dissimilar Nyquist and Arrhenius plots under 95% RH (Fig. 3e and corresponding data in Table 1). The E_a value was 0.39 eV (Fig. 3f), indicating that protons moved very smoothly through the Grotthuss mechanism over the entire temperature range. The interactive –OH groups of the HQ linker are helpful for reducing the length of proton conduction at the surfaces of the AOP-based frameworks, and the proton conductivity of AOP–HQ was enhanced to 1.31×10^{-2} S cm^{-1} at 90 °C, comparable with that of benchmark proton-conducting materials such as Nafion (>10^{-2} S cm^{-1}, Table S2). The AOP–HQ-type material also worked as a stable proton conductor, without a significant

decrease in the conductivity, for at least one week under 95% RH at 90 °C (Fig. 3g).

To probe the proton conduction mechanism dynamically, temperature-dependent FT-IR measurements were performed under 95% RH at 30 °C, 50 °C and 70 °C (Fig. S4). A broad absorption band attributed to hydrogen-bonded H_2O molecules was observed in the region of 3000–3600 cm^{-1} due to O–H stretching. In addition to the broad adsorption band centered at 3200–3400 cm^{-1} corresponding to hydrogen-bonded H_2O molecules, a shoulder at around 3450–3500 cm^{-1} was changed drastically upon elevating the temperature. This behavior is consistent with the proton conduction by the Grotthuss mechanism, in which proton hopping proceeds with continuous reorganization of hydrogen-bonded H_2O molecules.

To clarify the relationship between the adsorption behavior of H_2O molecules and proton conduction, the proton conductivity was analyzed as a function of the number of adsorbed H_2O molecules (Fig. 3h). The hydration state at the surfaces and/or inside the mesopores of AOP–HQ was roughly controlled by the humidity condition based on H_2O adsorption–desorption isotherm (Fig. S5). An increase by the pore filling with H_2O molecules was observed above $P/P_0 = 0.6$ in the H_2O adsorption branch, suggesting the transition point from the gradual adsorption of mesopore surfaces below 60% RH to the networking of hydrogen-bonded H_2O molecules at around 60% RH. However, protons were still conducted by the Grotthuss mechanism even under 60% RH, allowing the adsorption of H_2O molecules over the whole of the surface of the AOP–HQ, with an E_a value of 0.38 eV (Fig. 3i), identical to that observed under 95% RH (0.39 eV). Proton conductivity was also measured at temperatures ranging from 30 °C to 90 °C under 60% RH after exposure to 95% RH. The E_a value was 0.38 eV, which is quite similar to those observed under 60% RH (0.39 eV) and 95% RH (0.37 eV). The proton conductivity showed an exponential and positive correlation with the adsorbed amount of H_2O molecules under every condition, even when the temperature was increased to 90 °C, clearly demonstrating that the proton conductivity is governed primarily by the amount of confined H_2O molecules inside the mesopores, rather than the external RH condition.

3.3 Comparison of the proton conductivity between AOP–BP- and AOP–HQ- type mesoporous materials

The porosity data of AOP–BP and AOP–HQ were analogous to those observed for pure AlPO and other AOP-type mesoporous materials prepared using the same Pluronic P123 (Table S3),[33] which allows comparison of the significance of organic linkers, excluding the effect based on the physical structure of AOP-type mesoporous materials. The length of the –Ph–Ph– linker (≈1.07 nm) of AOP–BP is considerably longer than a typical distance between hydrogen-bonded adjacent H_2O molecules (≈0.28 nm). The continuous network of hydrogen-bonded H_2O molecules is restricted at the surfaces by the presence of the hydrophobic organic linkers. As reported previously,[33] the

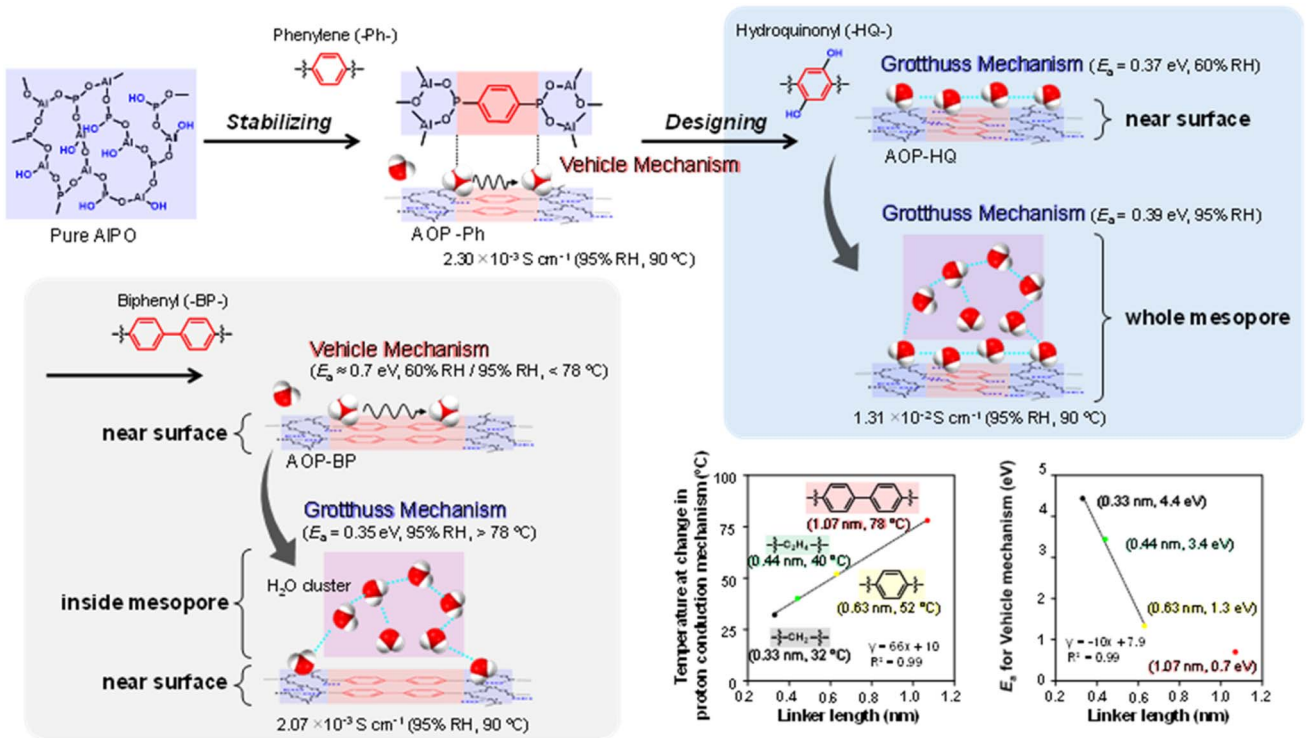

Fig. 4 Analysis of the AOP–BP- and AOP–HQ-type mesoporous materials. Schematic of the proton conduction mechanisms near the AOP–BP and AOP–HQ surfaces and inside the mesopores, with a comparison with the mechanism disclosed by using AOP–Ph (*e.g.*, the temperature at which a change in the proton conduction mechanism occurs, and the E_a value for the vehicle mechanism as a function of the length of organic linkers).

temperature at which the proton conduction mechanism changes strongly depends on the molecular size of the hydrophobic organic linkers (*e.g.*, $-CH_2-$, $-C_2H_4-$ and –Ph–). In the case of AOP–BP, the temperature was 78 °C under 95% RH, which is in good agreement with this trend (Fig. 4, bottom right). However, the E_a value (0.70 eV) for proton conduction by the vehicle mechanism was not plotted on the line of the linear relationship (Fig. 4, bottom right), possibly suggesting a decrease in the average length for the proton conduction by the random arrangement of –Ph–Ph– groups. Proton conduction above 78 °C under 95% RH is predominantly through the Grotthuss mechanism involving hydrogen-bonded H_2O clusters that do not interact with the surfaces of the AOP-based framework. Overall, the average distance for proton conduction should be adjusted to enhance the total proton conductivity inside the mesopores.

The proton conduction processes for AOP–BP and AOP–HQ near the AOP-based frameworks and inside the mesopores are compared in the schematics shown in Fig. 4. While the first layer of H_2O molecules, which is strongly attached to the AlO_4 units of the AOP-based framework, does not contribute to the proton conduction, the next layer of H_2O molecules can interact through hydrogen bonds and move as proton carriers. However, the hydrophobic and bulky organic linkers disturb the smooth proton-hopping vehicle conduction. Accordingly, the length of the proton-hopping should be adjusted by modifying the hydrophobic organic linkers. The proton conduction of AOP–HQ was then improved up to the order of 10^{-2} S cm^{-1} under 95% RH at 90 °C because the formation of a continuous network of hydrogen-bonded H_2O molecules was promoted by the incorporation of interactive –OH groups throughout the mesopore surfaces. To compare the surface hydrophilicity of AOP–BP and AOP–HQ more quantitatively, the adsorption behavior of H_2O was measured at a different temperature (40 °C, Fig. S6) to calculate the isosteric heat of adsorption (Q_{st}). The Q_{st} of AOP–HQ was much higher than that of AOP–BP in the low-coverage region, confirming a significant increase in the interaction of H_2O molecules by attaching –OH groups to the main –Ph– linkers.

4. Conclusion

AOP-type mesoporous materials (*e.g.*, AOP–BP and AOP–HQ) were constructed based on the rational design of organic linkers, such as strongly hydrophobic biphenyl ($-C_6H_4-C_6H_4-$ or –BP–) and interactive hydroquinonyl linkers ($-C_6H_2(OH)_2-$ or –HQ–). Consequently, the diffusion distance of H_2O molecules was reduced by the incorporation of –HQ– groups at the surfaces of the AOP-based frameworks, leading to the synthesis of a unique material exhibiting a superprotonic conductivity of 1.31×10^{-2} S cm^{-1} by ensuring efficient proton transport through the Grotthuss mechanism. The proton conductivity is comparable with those of state-of-the-art proton conductors, including Nafion-type materials (10^{-1}–10^{-2} S cm^{-1}) (Table S2). The proton conductivity would be improved further by optimizing the pathway to transport protons by modifying the design of the mesoporous structure (*e.g.*, pore size and pore dimension) as well as further tailoring the organic linkers (*e.g.*, functionalization with proton-donating groups such as $-SO_3H$ and –COOH).[44–46] The results highlight an important principle for the design of high-performance proton-conducting AOP-type materials. Although our latest study has mainly focused on improving the structural stability of AOP-based frameworks by introducing bulky and hydrophobic organic linkers,[33] the present data fully demonstrate that the chemical functionality of organic linkers can regulate the organization of confined H_2O molecules and thereby control the pathway by which the protons are transported. These guidelines will contribute to the practical development of AOP-type mesoporous frameworks as high-performance proton-conducting materials. A comprehensive evaluation of the practical properties, such as ion selectivity, chemical durability and mechanical strength, will be required to upgrade AOP-type mesoporous frameworks to device-level materials that can be used as true alternatives to Nafion.

Author contributions

Takahiro Ami: methodology, investigation, formal analysis, data curation, writing-original draft, and visualization; Kouki Oka: methodology, investigation, funding acquisition, resources, and writing-review and editing; Hitoshi Kasai: supervision and resources; and Tatsuo Kimura: conceptualization, methodology, investigation, writing-review and editing, validation, and visualization.

Conflicts of interest

The authors declare no conflicts of interest.

Data availability

The data supporting this article have been included as part of the supplementary information (SI). Supplementary information is available. See DOI: https://doi.org/10.1039/d5ta10085b.

Acknowledgements

This work was conducted with the partial support of the Cooperative Research Program of the "Network Joint Research Center for Materials and Devices (MEXT)". This work was also supported by the Japan Society for the Promotion of Science (JSPS) KAKENHI Grant Numbers 23K17945, 23H03827, 24K01552, and 24KJ1580. K. O. is grateful for the supports by the Environment Research and Technology Development Fund (JPMEERF20241RA4) of the Environmental Restoration and Conservation Agency provided by the Ministry of the Environment of Japan and the Advanced Research Program for Energy and Environmental Technologies (FY2025, JPNP14004) by the New Energy and Industrial Technology Development Organization (NEDO), Japan. K. O. also acknowledges the support from the Shorai Foundation for Science and Technology, the TEPCO Memorial Foundation, the Amano Industry Technology Laboratory, the Yamada Science Foundation, the Kenjiro Takayanagi

Foundation, the Kansai Research Foundation for Technology Promotion, the Yashima Environment Technology Foundation, the JACI Prize for Encouraging Young Researchers, the Foundation for Interaction in Science and Technology, the Iketani Science and Technology Foundation, and the Ichimura Foundation for New Technology.

References

1 Y. Nagao, *ChemElectroChem*, 2024, **11**, e202300846.
2 R. T. Liu, Z. L. Xu, F. M. Li, F. Y. Chen, J. Y. Yu, Y. Yan, Y. Chen and B. Y. Xia, *Chem. Soc. Rev.*, 2023, **52**, 5652–5683.
3 M. B. Hanif, S. Rauf, Z. Abadeen, K. Khan, Z. Tayyab, S. Qayyum, M. Mosiałek, Z. Shao, C.-X. Li and M. Motola, *Matter*, 2023, **6**, 1782–1830.
4 Y. M. Jo, D. H. Kim, J. Wang, J. J. Oppenheim and M. Dincă, *J. Am. Chem. Soc.*, 2024, **146**, 20213–20220.
5 J. Kim, S. Sengodan, S. Kim, O. Kwon, Y. Bu and G. Kim, *Renew. Sustain. Energy Rev.*, 2019, **109**, 606–618.
6 S. Mo, L. Du, Z. Huang, J. Chen, Y. Zhou, P. Wu, L. Meng, N. Wang, L. Xing, M. Zhao, Y. Yang, J. Tang, Y. Zou and S. Ye, *Electrochem. Energy Rev.*, 2023, **6**, 28.
7 W. Olbrich, T. Kadyk, U. Sauter, M. Eikerling and J. Gostick, *Sci. Rep.*, 2023, **13**, 14127.
8 H. Sei, H. Kasai and K. Oka, *Nanoscale Adv.*, 2025, **7**, 5501–5506.
9 R. Akai, H. Kasai and K. Oka, *Nanoscale*, 2025, **17**, 9920–9925.
10 T. Ami, K. Oka, S. Kitajima and N. Tohnai, *Angew. Chem., Int. Ed.*, 2024, **63**, e202407484.
11 D. W. Lim and H. Kitagawa, *Chem. Rev.*, 2020, **120**, 8416–8467.
12 H. Xu, S. Tao and D. Jiang, *Nature Mater.*, 2016, **15**, 722–726.
13 R. Saha and C. J. Gómez García, *Chem. Soc. Rev.*, 2024, **53**, 9490–9559.
14 W. Lee, H. Li, Z. Du and D. Feng, *Chem. Soc. Rev.*, 2024, **53**, 8182–8201.
15 D. W. Lim and H. Kitagawa, *Chem. Soc. Rev.*, 2021, **50**, 6349–6368.
16 Y. Lu, S. Zhou, C. Zhu, J. Zhou and X. Feng, *Chem. – Eur. J.*, 2025, **31**, e202501116.
17 P. Ramaswamy, N. E. Wong and G. K. H. Shimizu, *Chem. Soc. Rev.*, 2014, **43**, 5913–5932.
18 N. Agmon, *Chem. Phys. Lett.*, 1995, **244**, 456–462.
19 K. D. Kreuer, A. Rabenau and W. Weppner, *Angew. Chem., Int. Ed.*, 1982, **21**, 208–209.
20 S. S. Park, A. J. Rieth, C. H. Hendon and M. Dincă, *J. Am. Chem. Soc.*, 2018, **140**, 2016–2019.
21 K. Otake and H. Kitagawa, *Small*, 2021, **17**, 2006189.
22 M. Yang, L. Xiong, S. Ji, Y. Zhang, W. Shi, H. Li, P. Ma, J. Wang and J. Niu, *Chem. Mater.*, 2024, **36**, 8929–8935.
23 H. Wu, X. Wang, W. Wang, C. Liao, J. Wu, Z. Shao, Y. Zhou and Y. Li, *ACS Nano*, 2026, **20**, 657–671.
24 Y. Su, B. Li, Z. Wang, A. Legrand, T. Aoyama, S. Fu, Y. Wu, K. Otake, M. Bonn, H. I. Wang, Q. Liao, K. Urayama, S. Kitagawa, L. Huang, S. Furukawa and C. Gu, *J. Am. Chem. Soc.*, 2024, **146**, 15479–15487.
25 B. Chen, B. Li, Y. Su, J. Zhu, M. Gao, S. Xiong, P. Wang, Z. Wang, Q. Liao and C. Gu, *Angew. Chem., Int. Ed.*, 2025, **64**, e202515924.
26 S. Huang, Z. Yi, Z. Wang, T. Su, J. Wu, Z. Liang and J. Li, *Chem. Sci.*, 2026, **17**, 3259–3266.
27 S. Fang, Y. Liao, J. Tang, M. Tang, F. Zheng, Z. Pan, Y. Feng and G. Han, *Sci. Adv.*, 2025, **11**, eaeb0929.
28 J. Yu and R. Xu, *Chem. Soc. Rev.*, 2006, **35**, 593–604.
29 Y. Mu, Y. Wang, Y. Li, J. Li and J. Yu, *Chem. Commun.*, 2015, **51**, 2149–2151.
30 Y. Sun, Y. Yan, Y. Wang, Y. Li, J. Li and J. Yu, *Chem. Commun.*, 2015, **51**, 9317–9319.
31 C. Zhang, Y. Yan, Z. Huang, H. Shi, C. Zhang, X. Cao and J. Jiang, *Inorg. Chem. Commun.*, 2018, **96**, 165–169.
32 T. Kimura, Y. Sugahara and K. Kuroda, *Microporous Mesoporous Mater.*, 1998, **22**, 115–126.
33 T. Ami, K. Oka, H. Kasai and T. Kimura, *J. Mater. Chem. A*, 2026, **14**, 3863–3873.
34 T. Kimura, *Chem. Mater.*, 2003, **15**, 3742–3744.
35 T. Kimura, *Chem. Mater.*, 2005, **17**, 337–344.
36 T. Kimura, *Chem. Mater.*, 2005, **17**, 5521–5528.
37 T. Kimura, *Angew. Chem., Int. Ed.*, 2017, **129**, 13644–13648.
38 T. Kimura and Y. Yamauchi, *Chem.–Asian J.*, 2013, **8**, 160–167.
39 T. Kimura, K. Kato and Y. Yamauchi, *Chem. Commun.*, 2009, 4938–4940.
40 T. Kimura and K. Kato, *Microporous Mesoporous Mater.*, 2007, **101**, 207–213.
41 T. Kimura and K. Kato, *J. Mater. Chem.*, 2007, **17**, 559–566.
42 M. Thommes, K. Kaneko, A. V. Neimark, J. P. Olivier, F. Rodriguez-Reinoso, J. Rouquerol and K. S. W. Sing, *Pure Appl. Chem.*, 2015, **87**, 1051–1069.
43 A. Takamori and T. Kimura, *Langmuir*, 2023, **39**, 10680–10691.
44 Y. Guo, X. Zou, W. Li, Y. Hu, Z. Jin, Z. Sun, S. Gong, S. Guo and F. Yan, *J. Mater. Chem. A*, 2022, **10**, 6499–6507.
45 Y. Tian, G. Liang, T. Fan, J. Shang, S. Shang, Y. Ma, R. Matsuda, M. Liu, M. Wang, L. Li and S. Kitagawa, *Chem. Mater.*, 2019, **31**, 8494–8503.
46 R. l. Liu, D. Y. Wang, J. R. Shi and G. Li, *Coord. Chem. Rev.*, 2021, **431**, 213747.